

Duration of super-emitting oil and gas methane sources

Received: 1 May 2025

Accepted: 16 January 2026


Published online: 24 January 2026

 Check for updates

The duration of super-emitting events ($>100 \text{ kg h}^{-1}$) in oil and gas basins remains insufficiently understood but is key for reporting programs and mitigation strategies. Carbon Mapper conducted aerial surveys from April 30 to May 17, 2024, over the New Mexico Permian Basin, covering 276,000 wells, 1100 compressor stations, 175 gas processing plants, and 27,000 km of pipeline. We find over 500 super-emitting sources with 300 of these sources observed repeatedly across multiple days. We quantify total super emissions by integrating individual events with observationally constrained event durations (5.98–14.7 Gg CH_4) and compare to total emissions derived from basin average snapshots ($12.7 \pm 0.92 \text{ Gg CH}_4$). This gap between emission estimates is reconciled through assumptions on missed detections, characteristic event duration, detection frequency, and diurnal variability. Emission events generally lasted for at least 2 hours, and a small subset of sources (18 total), persistently emitted throughout the entire campaign, representing a near-term opportunity for mitigation. When compared to regional flux estimates derived from independent observations, we estimate super-emitters to contribute approximately 50% (37–73%) towards total emissions. Frequent wide-area monitoring is crucial for capturing rare super-emitter events that, together with other emission sources, drive basin-level variability and emission intensity.

Super-emitting methane sources ($>100 \text{ kg CH}_4 \text{ h}^{-1}$)¹ disproportionately contribute to total emissions in many large oil and gas producing basins^{2–4}, meaning that a relatively small fraction of infrastructure (–0.5–1%) may represent a large contribution to total emissions⁵. This outsized effect from super-emitters, therefore, in many cases, drives basin-level variability and intensity⁶. Super-emissions result from a variety of processes across the oil and gas supply chain, including what are commonly thought to be short-duration known process events (e.g., liquids unloadings, compressor blowdowns, other pressure releases) or process aberrations (e.g., faulty equipment, leaking infrastructure, other operational issues).

The contribution of super-emitters to net emissions on a regional basis remains difficult to parametrize in traditional bottom-up modeling approaches that quantify emissions using emission factors and activity data⁷, due to several key challenges. First, because super-emitters are rare relative to total infrastructure in a basin, robustly constraining the probability distributions of these events requires surveying a significant amount of representative infrastructure: identifying and characterizing events occurring at a rate of one in one hundred or one in one thousand necessitates tens to hundreds of thousands of site-level observations. Available ground-based facility-scale measurements, which have historically provided an emission

¹Carbon Mapper, 680 E Colorado Blvd, Pasadena, CA, USA. ²Department of Aeronautics and Astronautics, Massachusetts Institute of Technology, 77 Massachusetts Avenue, Cambridge, MA, USA. ³Center for Global Discovery and Conservation Science, Arizona State University, 808 S Rural Rd, Tempe, AZ, USA. ⁴Climate Sciences Department, Lawrence Berkeley National Laboratory, 1 Cyclotron Road, Berkeley, CA, USA. ✉ e-mail: @carbonmapper.org

factor foundation for some bottom-up inventories⁸, are limited in spatial coverage to date and collectively, multiple measurement campaigns have resulted in only a few thousand site-level observations across multiple basins⁸. Second, many ground-based emissions monitoring technologies have not been rigorously validated for the quantification of facility-scale emissions at high emission rates. In one blinded controlled-release study, ground-based continuous monitors severely underestimated super-emitter sized events, likely due to the challenges in quantifying and accounting for transport dynamics and the vertical structure of methane plumes⁹. These two factors (spatial sampling and quantification bias) independently complicate unbiased characterization of super-emissions within traditional bottom-up inventories⁸ and generally have the effect of reducing the net influence of super-emitters against regional net emission totals⁸.

Unbiased treatment of facility-scale measurements from broad areas can clarify the relative role of super-emitters against net regional emissions. Measurement-informed inventories successfully prototyped in previous studies perform this function of disentangling larger emitter contributions compared to other sources^{2,10,11}, and provide an empirical and statistical mechanism to reconcile the bottom-up and top-down emission estimates at the basin level. A key assumption in these analyses is that population statistics from a single scan of a basin provide generalizable information about the prevalence and contribution of super-emitters. Aerial measurement technologies, such as fixed-wing LiDAR¹² and passive remote sensing^{13–15}, have been pivotal to these studies, enabling efficient observation of the thousands to hundreds of thousands of sites needed to understand the dynamics of super-emitters. To date, aerial quantification shows little to no systematic bias at high emission rates when evaluated against blinded controlled releases^{16,17}. Other studies have quantified the super-emitter contribution to total emissions through integration of data from multiple observing systems (e.g., tall towers, aircraft, satellites) that separately quantify total emission fluxes and super-emitting sources^{3,5}.

Though useful for the application of basin-level inventory accounting, such approaches provide limited information regarding the true intermittency and duration of emission events at individual sites. This is of great importance for reporting programs such as the U.S. Greenhouse Gas Reporting Program (GHGRP), which requires operators to report methane emissions from large sources to the U.S. Environmental Protection Agency (EPA). In 2024, EPA updated the oil and gas reporting protocols of the GHGRP (Subpart W), requiring the reporting of “other large releases” above 100 kg h⁻¹ (i.e., super-emitters). Similarly, the United Nations Oil and Gas Methane Partnership 2.0 (OGMP) provides a measurement-based framework for oil and gas companies to report and track their emissions with site-level measurements, with the goal of improving accountability and progress towards emission mitigation targets. In this framework, understanding the intermittency and duration of emissions is essential for accurate accounting and reconciliation.

Given the complexity of oil and gas systems, relatively little public data exists characterizing representative emission durations across general classes of operations. One study, performed at two midstream compressor stations in New York using continuous emissions monitoring system (CEMS) observations and operators reports, estimated average super-emitter durations of 30 min, with a minority but significant number of events lasting longer than 5 h¹⁸. However, super-emitter events span various infrastructure types and supply-chain segments (e.g., tanks, flares, pipelines), and are operator dependent. A separate study¹⁴ based on broad aircraft surveys over a six-week period found a class of persistently super-emitting infrastructure in the Permian Basin, associated with multiple infrastructure types, indicating that some event may have durations longer than sub-hour.

In this study, we conducted intensive aerial surveys over a three-week period between April and May 2024 on the New Mexico side of the Permian Basin. The campaign was specifically designed to address

questions related to both the intensity and duration of super-emitters across all infrastructure and supply chain categories within the domain. Thousands of infrastructure elements were surveyed daily, often multiple times per day, and over multiple days. We identify hundreds of super-emitter events, estimate their durations based purely on observations, and attribute each event to specific infrastructure using high-resolution visible imagery and geographic information system (GIS) datasets. We compare the sub-basin level emission estimate to an emission estimate derived through integration of individual events, based on their calculated event durations. Our findings reveal that a small but significant fraction of super-emitter events were persistent throughout the campaign, highlighting the potential for substantial near-term methane mitigation.

Results

Survey design and methane detection limit

Carbon Mapper conducted an airborne campaign with the Global Airborne Observatory (GAO; <https://asnerlab.org/projects/global-airborne-observatory/>) over the New Mexico (NM) side of the Permian Basin between April 30–May 17, 2024 (Fig. 1). The survey was designed for two primary objectives: (1) to cover the vast majority of NM oil and gas infrastructure and production at least once to estimate basin-level emissions from super-emitters (referred to here as the “Full Region”), and (2) to focus on high-production regions with multiple revisits over subsections of the basin to quantify the duration of super-emitter events. These intensive areas of interest were subdivided into two regions, the “West Box” and the “East Box.”

The Full Region covers 12,000 km² which, according to the Rextag oil and gas infrastructure database (<https://www.rextag.com>), includes 67,000 wells, 98% of NM Permian oil Production, and 98% of NM Permian gas production, along with 295 compressor stations and 45 gas processing plants. During the campaign, the Full Region was mapped wall-to-wall, meaning complete coverage of all oil and gas infrastructure, including 17,000 miles of gathering and transmission pipelines. The West Box covers 1,200 km², including 6400 wells, 16% of NM Permian oil production, and 22% of NM Permian gas production. It was mapped multiple times per day on May 1, 13, and 15, with partial coverage on 4 additional flight days. The East Box also covers 1,200 km², including 9,200 wells, 35% of NM Permian oil production, and 42% of NM Permian gas production. It was mapped multiple times per day on April 30 and May 14, with partial coverage on 4 additional flight days. Together, we estimate over 200,000 site-level observations were made during the course of the campaign, when accounting for multiple survey revisits.

Carbon Mapper processes GAO radiance to identify, geolocate, and quantify large methane emission sources at sub-facility scales. These algorithms have been rigorously tested through blinded controlled release experiments, with releases ranging from 5.0 to 1500 kg per hour¹⁶. The 90% probability of detection, hereafter referred to as detection limit (DL), in these controlled environments ranges between 10–45 kg per hour¹⁹. Alternatively, assuming a power-law distribution of oil and gas emissions in a basin^{12,13}, one can estimate the DL from the data by identifying the emission level at which the frequency of detections diverges from a power-law distribution. During the course of the campaign, 1380 plumes were detected, and their frequency distribution suggests a DL between 70–150 kg h⁻¹ (Details provided in the Supplementary Notes). Therefore, for the purpose of this study, we assume near-full detection sensitivity to the super-emitter class (>100 kg h⁻¹) of emissions. All plumes detected and summarized in this survey were determined to originate from the oil and gas sector.

Contribution of super-emitters to total regional emissions

Figure 2a shows the locations of methane detections. To aggregate these detections into a domain-level super-emitter emission estimate (here, the NM Permian Basin), we must account for uneven temporal

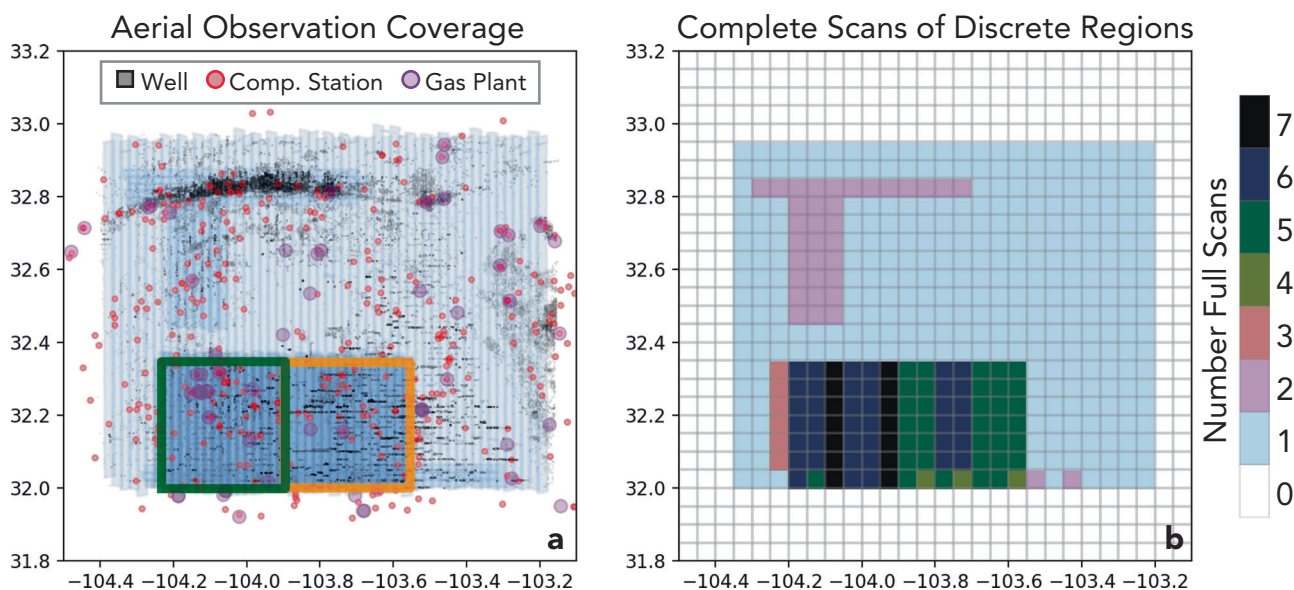


Fig. 1 | Observation coverage of aerial survey. **a** Flight outline of observed areas by Carbon Mapper, with Rextag-reported well-sites, compressor stations, and gas plants overlaid. The green and orange square polygons represent areas of high

production and intensive aerial surveys. **b** Number of complete observational revisits across discrete $0.05 \times 0.05^\circ$ regions within the basin.

sampling across the domain. This is done by dividing the entire survey domain into discrete $0.05^\circ \times 0.05^\circ$ ($\approx 5 \times 5 \text{ km}^2$) grid cells and summing detected emissions per complete observational scan of each grid cell. For example, if a grid cell was surveyed in its entirety five times, there would be five independent emission estimates (“sums” of plumes) for that grid cell. In cases where an emission source was observed twice in rapid succession due to overlaps in airborne image acquisition during a single scan, only the first source observation of that source is included in the scan’s emission total.

We then derive a campaign-average emission rate for each grid cell by averaging all independent emission estimates for that grid cell. Applying this across all grid cells produces a heatmap of super-emissions within the surveyed areas (Fig. 2b). Uncertainties for each grid cell (1σ) are calculated by first summing individual plume emission uncertainties within a single scan. There may be a correlation between the emission quantification of two independent plumes detected in a single scan that could be caused by errors in wind speed and concentration retrievals, hence the choice of linear uncertainty summation. To estimate uncertainty in the mean estimate across all independent scans of a grid cell, we sum in quadrature the uncertainties across all scans for that grid cell, as each individual scan is spaced by at least several hours and consists of independent concentration retrievals. As each grid is assumed to be an independent contributor to the total emissions within the domain, we estimate regional emissions (e.g., the Full Region) by summing mean emissions for all relevant grid cells that pertain to that domain, with uncertainties combined in quadrature. Using this method, we estimate $0.65 \pm 0.06 \text{ Tg a}^{-1}$ for the Full Region and $0.27 \pm 0.02 \text{ Tg a}^{-1}$ for the combined West + East Boxes (hereafter referred to as the “Intensive Box”). A sensitivity analysis of grid cell resolution and alternative emission quantification procedures is described in the Supplementary Notes.

We compare regional super-emitter estimates to total CH_4 emission fluxes derived from satellite observations by the Tropospheric Monitoring Instrument (TROPOMI) onboard the Sentinel-5p satellite²⁰. We use the Integrated Methane Inversion (IMI) system, previously applied to the Permian Basin^{21,22} (“Methods”), to relate coarse ($5.5 \times 7 \text{ km}^2$) atmospheric concentration datasets retrieved from TROPOMI to net emission fluxes ($25 \times 25 \text{ km}^2$ resolution) through inverse atmospheric transport modeling regularized by a Bayesian prior

emission estimate (“Methods”). Assimilating TROPOMI observations during the aircraft campaign period (Fig. 2c), we find the total methane flux from this region of the Permian to be $1.28 \pm 0.31 \text{ Tg a}^{-1}$, where the reported uncertainty here represents the one-sigma variability in weekly TROPOMI flux estimates over the campaign.

Comparison of total flux to sources detected aerially suggests that approximately 50% of emissions were contributed by super-emitters, or 37–73% when including 1σ uncertainties from both airborne and IMI quantification approaches. This partitioning between super-emitters and other emission sources is consistent with previous analyses^{13–15}. The number of super-emitting sources is small relative to the total infrastructure surveyed: 464 emission sources were detected at well sites, compressor stations, or gas plants, representing approximately 0.7% of infrastructure according to the Rextag database, and 65 pipeline sources (gathering and transmission) were detected, representing one detection per 420 kilometers of pipeline. This highlights the disproportionate contribution of super-emitters to regional emissions in the New Mexico Permian Basin.

The multiple revisits of the Intensive Box show substantial variability in the “heavy-tail” of emission distributions across comprehensive scans. Figure 3a shows cumulative emission distributions for each complete scan of the Intensive Box. Emissions quantified at instantaneous rates above 1000 kg h^{-1} account for 10–20% of total super-emissions for the first and second scans, while detections over this threshold account for 30–40% of total super-emissions for the third and fourth scans. Figure 3b shows the total emissions for each observation scan within the Intensive Box. Similarly, the total emissions estimated from the first and second scans ($0.21\text{--}0.22 \text{ Tg a}^{-1}$) are 30–40% lower than those estimated from the third and fourth scans ($0.32\text{--}0.35 \text{ Tg a}^{-1}$).

There are multiple possible explanations for this observed variability. One possibility is inherent temporal variability in the underlying probability of super-emissions within a dense and complex basin like the Permian. While we cannot rule this out, another possibility is that although each scan includes measurements of all assets in the Intensive Box, the sample size remains relatively small, and the observed variability is simply due to expected statistical variability. Each scan of the Intensive Box resulted in 80–116 super-emitter detections, but only 2–11 detections above 1000 kg h^{-1} . Given that these emissions above 1000 kg h^{-1} can

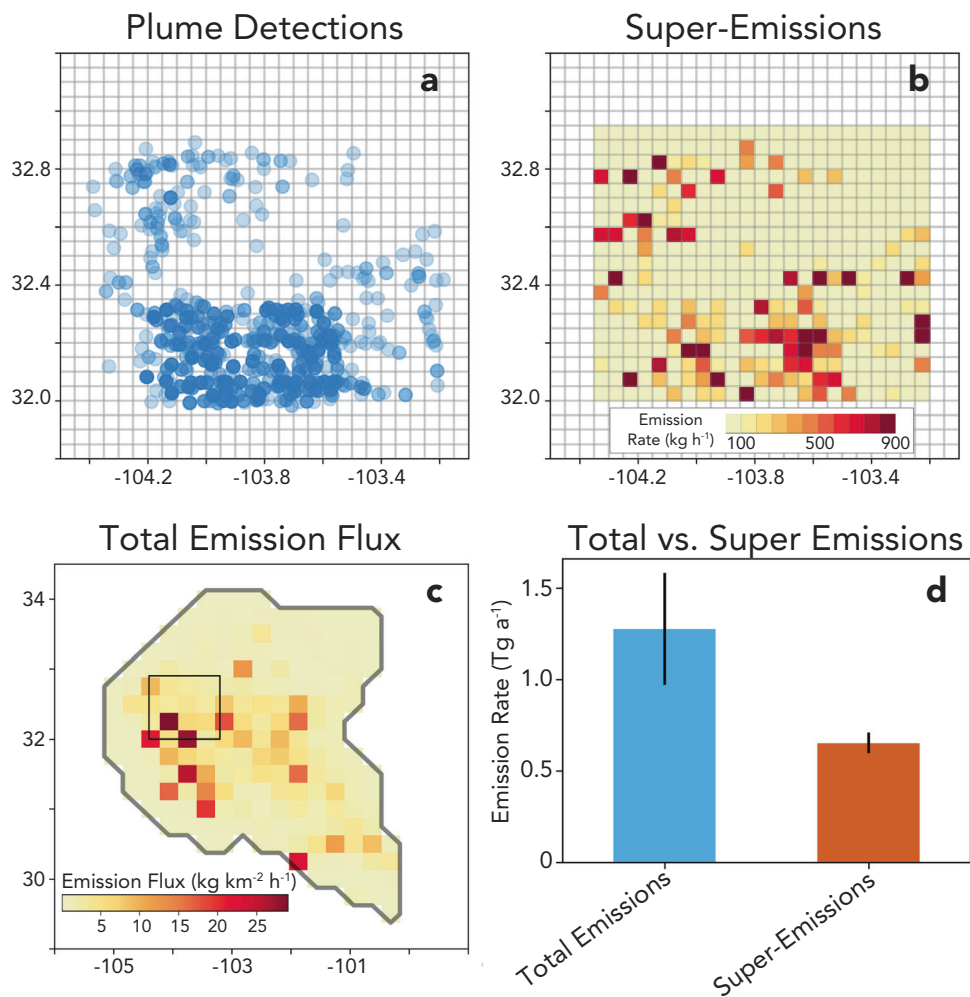


Fig. 2 | Methane results from the survey. **a** Locations of aerial plume detections. **b** Plume detections averaged to $0.05^\circ \times 0.05^\circ$ grid cells, following the methods described in the text. **c** Total emission fluxes ($25 \times 25 \text{ km}^2$) from the Permian Basin, derived from inversion of TROPOMI satellite observations. The inset black box represents the area surveyed during the airborne campaign. **d** Comparison between emissions estimated by TROPOMI (inset black box in (c)) and super-emissions within the same area (b)), where uncertainties represent one standard deviation.

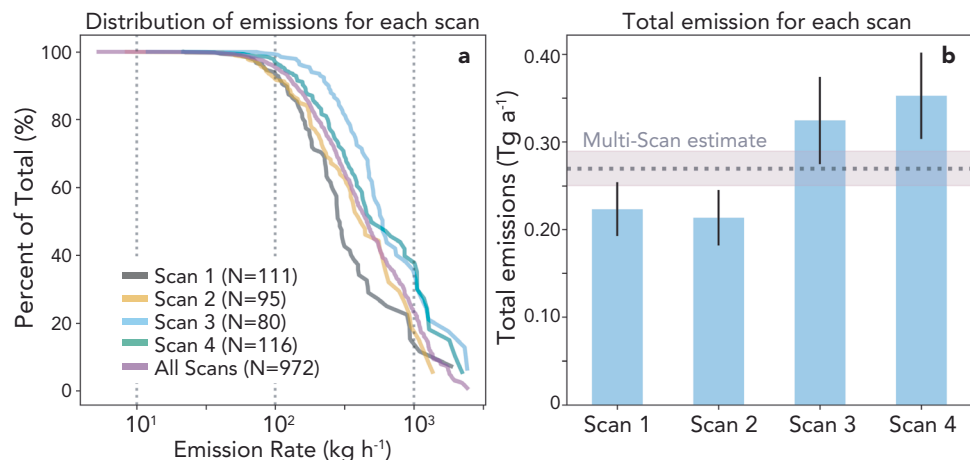


Fig. 3 | Variability assessment of Intensive Box. **a** Cumulative distributions of emissions in the Intensive Box for each observational scan. **b** Total emissions in the Intensive Box for each observational scan. The horizontal bar represents the estimated total emissions for the Intensive Box following the multi-scan aggregation procedure described in the text and shown in Fig. 2. Uncertainties represent one standard deviation.

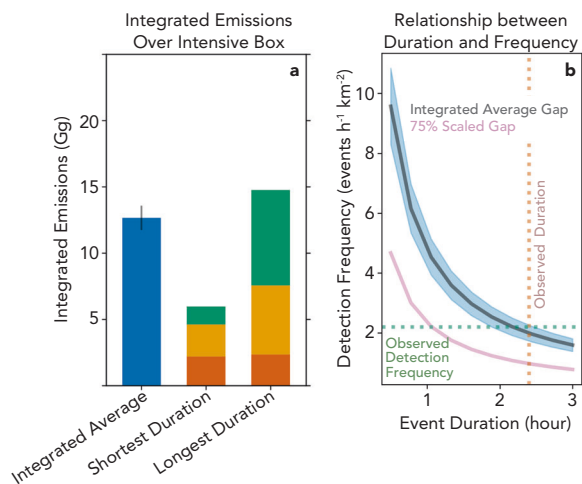


Fig. 4 | Results from estimating durations of super-emitter events in the Intensive Box. **a** Total emissions from the Intensive Box (West and East Boxes combined, see Fig. 1), integrated over the course of aerial survey, assuming either constant emissions (“Integrated Average”, left bar, 1σ uncertainty), or integration from detected sources using the shortest or longest emission durations constrained directly by aerial observations (middle and right bars, respectively). **b** Relationship between detection frequency and event duration during hours of non-observation needed to reconcile the emission gap estimate, derived by differencing the Integrated Average and Shortest Duration estimate (**a**) and described by Eq. (1).

constitute up to 40% of the super-emitter total, it is entirely possible that the observed variability is largely explained by small sample size effects. When including all scans, the resulting distribution becomes smoother and more robust, with 972 total detections and 49 detections greater than 1000 kg h^{-1} contributing 23% to total super-emissions. This suggests that for basins with emissions size distributions similar to the Permian, reliably quantifying the upper tail of the distribution ($>1000 \text{ kg h}^{-1}$), even within a relatively large sub-region, requires measuring all assets multiple times. Figure 3 is suggestive that four scans are sufficient to capture the rightmost tail of the distribution, but further study with increased spatiotemporal sampling can improve understanding of observational requirements for best characterization of this portion of the distribution. For the middle section of the emissions size distribution, comprising emissions from approximately $100\text{--}1000 \text{ kg h}^{-1}$, observed results are more stable. Across the first four scans, estimated total emissions below 1000 kg h^{-1} range from $0.18\text{--}0.22 \text{ Tg a}^{-1}$, showing less variability than when considering the full emission distribution. This suggests that for emissions in this size range, a single comprehensive scan may be sufficient, at least for a region with an emissions size distribution similar to that of the New Mexico Permian.

Comparing time-integrated to time-averaged emission totals

Through repeat observations, we derive estimates for characteristic super-emitter event durations, and estimate that most events are greater than two hours, with some events lasting days. We arrive at this conclusion through analysis and reconciliation of several related but independent metrics: First, we track and estimate bounds for each super-emitter event’s start and end time over the course of the campaign from observations alone. Second, we quantify spatial detection frequencies (number of events per km^2 per hour surveyed) to understand the prevalence and spatial distribution of super-emitter events within the surveyed area. Third, for days where we sampled the East and West Boxes intensively, we estimate the probability of detection

reoccurrence for sources that were observed subsequently minutes to hours after the first detection. These three metrics together are used to compare against the $0.27 \pm 0.02 \text{ Tg a}^{-1}$ super-emission aggregate rate estimated for the Intensive Box, where it is assumed to be emitting at that rate continuously during the entirety of the campaign.

We bound super-emitter events start and end times through observations. We detected 1380 individual plumes from 529 sources during the campaign. The Intensive Box contains 274 sources, from which we estimate 369 super-emitter events (“Methods”). A total of 174 super-emitter events both started and ended during the campaign (“finite” events); 18 emitted for the entirety of the campaign (“unbounded” events); and 177 either started during the campaign but were still emitting at the campaign’s end or were already emitting at the campaign start but ended before the campaign’s conclusion (“mixed” events). We associate durations for each super-emitter event, bounded by the shortest and longest possible event times estimated by direct observation (“Methods”). The median shortest and median longest duration for finite events (respectively) is 2.4 to 145 h, for mixed events is 0.14 to 129 h, and for unbounded events is 387 to 411 h. The distribution of shortest and longest event durations (hours) for each class of event is shown in Supplementary Figs. 22–25.

We integrate the total emission for each event using the average emission rate estimated across all detections for that event and the estimated event duration. Figure 4 shows the sum of emissions integrated from all detected events in the Intensive Box across the full campaign, using both shortest and longest possible event durations, and compares to the basin-level emission estimate ($0.27 \pm 0.02 \text{ Tg a}^{-1}$), which is assumed constant and integrated across the entirety of the campaign ($12.7 \pm 0.92 \text{ Gg}$), hereafter referred to as “Integrated Average.” Integration of super-emitter events using the shortest duration results in 5.98 Gg, with 2.18 Gg (36%) from unbounded events, 2.44 Gg (41%) from mixed events, and 1.36 Gg (23%) from finite events. Integration using the longest durations results in higher total emissions (14.7 Gg), with 2.33 Gg (16%) from unbounded events, 5.21 Gg (35%) from mixed events, and 7.20 Gg (49%) from finite events.

The Integrated Average is assumed to represent an unbiased estimate of total methane released during the survey, i.e., it statistically accounts for sources missed by the aircraft during hours of non-observation². The time-integrated estimates under the shortest and longest duration assumptions represent the total emission contributions of events directly observed by the aircraft. Therefore, the difference between the Integrated Average and time-integrated estimates represents an estimate of emissions anticipated but not directly observed. The difference between the Integrated Average estimate in Fig. 3a and the shortest-duration time-integrated estimate reveals a 6.67 Gg gap in total emission estimates. In contrast, the difference between the Integrated Average and the longest-duration time-integrated estimate results in an unrealistic -2.0 Gg surplus in emissions, indicating that the longest estimated event durations derived from observations are likely too large. Several single-detection finite events do not have a follow-up observation for an extended period, often days, which likely artificially inflates the longest duration estimate.

The 6.67 Gg gap between the Integrated Average and the shortest-duration time-integrated estimate in Fig. 4 is indicative of how aggregation of site-level reporting could potentially represent a biased estimate of regional emissions. This potential bias, or gap, is caused by (1) inaccurate estimation of event durations, and/or (2) incomplete or missing emission information from a set of sites that were emitting for some period of time. Therefore, to reconcile the 6.67 Gg gap, we must further assess the representativeness of each of these factors. Specifically, the emission gap (G ; units kg) between the Integrated Average and the shortest-duration time-integrated estimate (i.e., 6.67 Gg) can be reconciled through a set of non-observed events emitting at a characteristic emission rate Q (units kg h^{-1}), and characteristic duration D (units hours), during non-observed hours T (units hours), over an

area A (km^2), related to the spatiotemporal frequency of events F (units events $\text{km}^{-2} \text{h}^{-1}$) via the following relationship:

$$F = \frac{G}{D \cdot Q \cdot T \cdot A} \quad (1)$$

Figure 4b shows the outcome of F from Eq. (1) assuming $Q = 150 \text{ kg h}^{-1}$ (e.g., the mode of the emission distribution in Supplementary Fig. 1), and $G = 6.67 \text{ Gg}$, using a variety of event duration values D . As expected and shown, if characteristic event durations are assumed to be longer, then fewer events must have occurred to reconcile the 6.67 Gg gap (and vice-versa). To estimate a single representative value of D for this campaign, we analyzed sources with multiple observations per day, where the spacing between the first plume detection and last observation (regardless of subsequent detection) was at least two hours (i.e., April 30, May 1, May 14–15; 230 sources total). Supplementary Fig. 25 shows the distribution of time differences between first and last detection for these sources. Sixty-nine percent of plume detections were followed by repeat detections at least two hours later, with a median duration of 2.4 h. The 2.4-h median is primarily set by observation revisit time, as only 2% of sources were observed more than three hours after the initial detection. Restricting this analysis to sources previously classified as finite (77 sources total) yields similar results, with a median duration of 2.3 h. We also estimate F for this campaign through analysis of plume detection timestamps and full-image acquisition geometries, and find that we detected 2.2 short-duration finite super-emitter events $\text{h}^{-1} \text{ km}^{-2}$.

We test the likelihood of longer (2.4 h) versus shorter (8.3 min; the minimum finite event duration quantified in this study) characteristic timescales for short-duration finite events by application of Eq. (1) and Fig. 4b compared to the spatial detection frequency F that we observed during the campaign. Assuming finite super-emitter events characteristically last 8.3 min in Eq. (1) translates to a detection frequency (F) of 35 events $\text{h}^{-1} \text{ km}^{-2}$ surveyed, which is 16 times higher than the detection frequency we actually observed during the campaign. When instead 2.4 h are assumed as a characteristic event duration, Eq. (1) estimates 2.0 events $\text{h}^{-1} \text{ km}^{-2}$ surveyed, which is very close to 2.2 events $\text{h}^{-1} \text{ km}^{-2}$ we observed during the survey. This point is visually conveyed in Fig. 4b - the modeled non-observed event duration and detection frequencies from Eq. (1) nearly intersect the observed duration (2.4 h) and detection frequency (2.2 events $\text{h}^{-1} \text{ km}^{-2}$) values. This intersection supports the assumption that the population statistics observed during the survey likely continued similarly during non-observation hours. If, instead, one assumes shorter event durations, this implies a much higher frequency of super-emitter events during periods of non-observation than was actually observed during the survey, which may be unlikely.

These results underscore the importance of proper duration estimation for site-level accounting across the complex set of processes that lead to super-emissions. Assuming a single duration value for all super-emitter events can severely bias the aggregate accounting of emissions. For example, if we apply a 2.4 h duration, the value derived for finite short-lived events, to all detected events in this study, the regional aggregate emission estimate would be 0.21 Gg, whereas applying a single 72 h duration to all detected events would result in 6.4 Gg, not dissimilar to the shortest-duration integrated estimate in Fig. 4a. Future study could connect durations we derived to operator-level information where available, so that more characteristic durations can be applied appropriately to specific processes. However, given the continuing uncertainty, we do find clear evidence in this study that a small but significant fraction of super-emitters last days to weeks, and that short-lived super-emitter events likely persist for at least 2 h.

Diurnal variability may also drive the size of the emission gap. A previous study using a network of continuously observing towers in the Permian showed that daytime-centric measurement studies may

overestimate emissions in the Permian by as much as 27%, due to unaccounted diurnal variability²³. To account for this, we can scale G in Eq. (1) by 0.73 to represent possible diurnal effects. However, as shown in Fig. 4b (purple curve), this adjustment eliminates the intersection point between candidate duration/frequency pairs and independent duration/frequency estimates, suggesting some combination of shorter event durations or fewer detections during unobserved hours. Ultimately, further study with more continuous observations can help reduce lingering uncertainty. Since detection frequency and event duration are closely linked, future studies must balance observing systems that maximize spatial coverage with those that maximize temporal coverage.

Super-emitter duration by infrastructure type

Each source was attributed to broad infrastructure categories using simultaneously acquired 5 m visible imagery, asynchronously collected high resolution visible imagery (<1 m) from Mapbox (www.mapbox.com), and the Rextag GIS database (see Supplementary Notes). Sources were assigned to the following infrastructure categories: compressors, flares, tanks, and pipelines (gathering or transmission). We also classified sources that do not fall into those categories but that were clearly located within the footprint of a well site or gas plant as “other well site” and “other gas plant,” respectively. Lastly, any sources for which a clear infrastructure designation could not be made, due to a combination of incomplete GIS information or unclear visible imagery, were classified as “other.” Fig. 5a shows the breakdown of sources attributed to infrastructure categories across both the entire survey domain and the Intensive Box. Compressors constitute the majority of detected sources across the full survey domain (27%) and represent a significant fraction of sources (25–39%) across duration categories in the Intensive Box. Combined with pipelines, these sources together make up 39% of all sources detected. These results highlight sustained, large emission activity associated with gathering and boosting activities in the Permian, a pattern that has been noted in multiple measurement surveys dating back to 2019^{14,24,25}. After compressors, the most prevalent source categories are other well-sites (24%), tanks (22%), pipelines (12%), flares (11%), and other gas plant sources (2%).

Across super-emitter event duration classes within the Intensive Box, there is some slight variation in infrastructure prevalence (Fig. 5b). For example, among finite events, other well-site emissions are more prevalent (36% of all finite sources) than compressors (25%), whereas across unbounded events, well-site events are much less prevalent (6% of unbounded sources) compared to compressors (39%). Using a related metric, source persistence or detection frequency (number of detections divided by number of overpasses) (Fig. 5c), other well-site sources are more intermittent (median 25%) than any other source category. This, along with their high prevalence among finite-duration events, suggests that these detections are generally shorter-lived and potentially associated with planned or known operations. In contrast, attributed tank sources, many of which are located at well-sites, are more persistent (40%) and have lower prevalence among finite events than other well-site emissions: 22% of tank sources pertain to the finite class, compared to 36% of other well-site emissions. Emissions from tanks can result from a variety of causes, ranging from short-lived safety events (e.g., flashings) to longer-lived operation inefficiencies (e.g., open hatches, leaks). The observations of more persistent, longer-lived tank emission suggests that a subset of these sources pertain to the latter category, meaning that focused attention on these sources could potentially lead to significant emission reduction.

Discussion

Facility-scale point source super-emitter observations support multiple use cases: (1) improving characterization of basin-scale emissions, (2) enhancing internal or external operator reporting of emissions, and

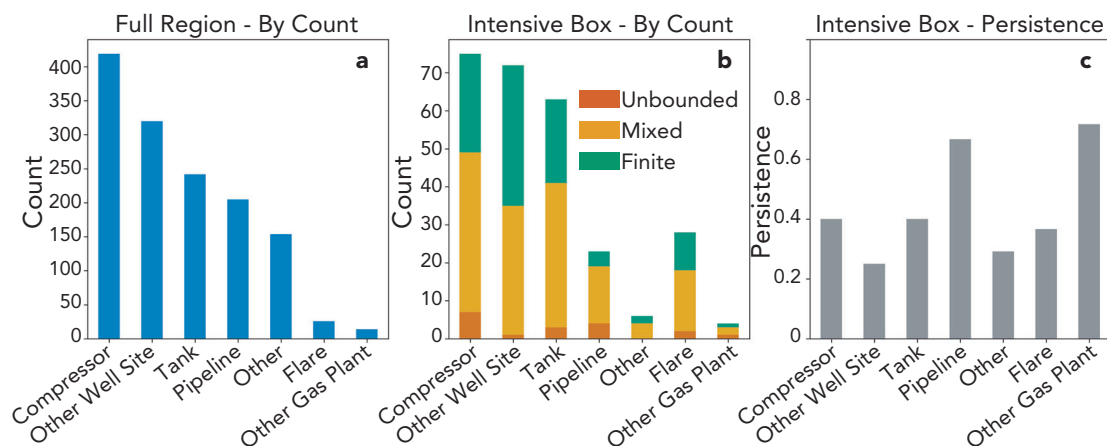


Fig. 5 | Infrastructure counts for detected sources during the campaign with associated source persistence. a Infrastructure counts for sources across the entire survey spatial domain. **b** Infrastructure counts for sources in the Intensive

Box, broken out by super-emitter duration category. **c** Median persistence (number of detections divided by number of observations) for infrastructure in the Intensive Box.

(3) identifying and prioritizing emission mitigation opportunities. For the first use case (basin-scale emission estimation), understanding the contribution of super-emissions to the basin total requires several key observational constraints, including detection sensitivity to a critical range of super-emitters (i.e., DL $\sim 100 \text{ kg h}^{-1}$) and broad spatial sampling across a basin to capture the inherent low frequency of these emitters. In the absence of these two observing requirements, layers of inference can be used to fill in spatial and sensitivity gaps, but such inference may introduce bias and misrepresent the impact of large emission sources on regional emissions. This study observed all infrastructure and production on the New Mexico side of the Permian Basin during an 18-day campaign, capturing representative statistics on super-emitters during the observation period. We estimate that super-emitters account for 50% (37–73% range) of total emissions in this domain, highlighting the disproportionate impact, consistent with previous studies using independent measurement systems^{2,15,26}.

Reporting programs like GHGRP Subpart W rely on event duration for the reporting of large emission events. Operator information from known process events or data from supervisory control and data acquisition (SCADA) systems can be valuable for estimating event durations. However, in many cases, operators may not have detailed information from all emission events²⁷, especially in instances of unexpected leaks or malfunctions. In these cases, atmospheric observations can be useful for filling gaps by independently quantifying event durations. Nevertheless, a fundamental limitation of current observing systems is the inability to simultaneously provide the spatial coverage needed to estimate basin-level super-emitter contributions and the temporal resolution required to constrain the duration of individually events. In this study, we estimated event durations directly from aerial observations, focusing on areas of the Permian that were observed repeatedly (the Intensive Box). Integration of these events using the shortest and longest possible event durations results in total emissions ranging from 5.98 to 14.7 Gg CH_4 . When isolating to the unbounded category, where we have the greatest confidence in emission duration, we find that mitigation of these 18 sources, most of which are from compressors, would result in sizable emission and cost reductions ($6180 \pm 2100 \text{ kg h}^{-1}$).

Overall, we demonstrated that frequent wide-area monitoring of oil and gas basins for super-emitters uncovers a diverse array of processes, infrastructure types, emission magnitudes, and event durations. We find evidence suggesting that characteristic super-emitter durations are often on the scale of hours. Ultimately, leveraging a tiered observing system that uses multiple technologies and vetted data sources (e.g., operator reports) can further reduce quantification

uncertainty across the oil and gas supply chain. In particular, developing algorithms or leveraging new technology that can quantify and attribute site-level emissions at a critical set of sites basin-wide, with high temporal sampling, and reliably low detection limits can be pivotal for further improved characterization of emission dynamics for most sources that make up regional emissions. Some aerial survey deployments can provide both the spatial breadth and revisit frequency needed to build evidence of characteristic duration and emission magnitude, which are key for validating reporting programs and identifying areas for immediate mitigation.

Methods

Super-emitter event duration calculation

Super-emitter event durations are estimated directly from repeat aerial observations, with a focus on the East and West Boxes, where multiple overpasses were made over the course of the campaign. To classify site-level sources, we cluster plume detections in space, time, and by infrastructure using the Density-Based Spatial Clustering of Applications with Noise (DBSCAN) algorithm with a local neighborhood of 250-m²⁸. DBSCAN is an unsupervised clustering algorithm that groups closely packed points in a dataset together. We then classify super-emitter events by the binary detection outcome of each observation for each source. If a detection follows a non-detection, it constitutes the start of a new event. If a non-detection follows a detection, it constitutes the end of an event. A single emission source can therefore have multiple super-emitter events. For events whose first or last observation results in a detection (or both), the duration of the event is unbounded, meaning we have no information to suggest how much longer earlier or later relative to the campaign, the emission event started or ended, respectively.

This process of super-emitter event identification from direct observation results in four categories: (1) *finite*, meaning we observed the beginning and end of the event; (2) *unbounded start*, meaning the first observation resulted in a detection, but the event ended before the campaign concluded; (3) *unbounded end*, meaning the event was observed to start during the campaign, but the last observation was a detection; and (4) *unbounded*, meaning that all observations resulted in a detection. For the sake of comparison in this manuscript, we group unbounded end and unbounded start events together to make a *mixed* category.

Durations for each event are constrained to the shortest and longest possible lengths based on observations. For example, if a source was observed four times, and only the second and third observations resulted in detections, this would constitute a finite

event, with the shortest possible duration being the time elapsed between the second and third observations and the longest possible duration being the time between the first and fourth observations. In this example, it is possible that the source temporarily stopped emitting between the second and third observations, which was not observed. Had it been observed, it would have resulted in two distinct events with total durations shorter than this single event duration. However, this potential bias is assumed to be negated by cases of non-detections between successive observations when, in reality, there may have been a temporary super-emitter event that went undetected. Therefore, for the purpose of this study, we follow the duration estimation procedure as described above and assume that missed detections and non-detections between site observations are equally likely. Further study with distributed CEMS systems or more intensive aerial surveys could reduce lingering uncertainty related to these assumptions, presuming they are representative of all infrastructure in a basin.

For unbounded cases, we restrict the duration to either the campaign start or end for the purpose of understanding emissions strictly within the time domain of the aerial campaign itself. For example, for an unbounded start event where the first observation resulted in a detection and the second observation a non-detection, the shortest possible duration would be near-instantaneous given the single snapshot detection, and the longest possible duration would be the time elapsed between the start of the campaign (first observation of any site) and the second observation. Technically, the shortest duration could be estimated from a two-dimensional plume image itself, as the concentration at the tail of an observed plume must have traveled from the source's origin over a period of time. However, rigorous estimation of these length scales would require complex atmospheric modeling, and in cases of remote sensing, the true spatial atmospheric distribution of a plume is anticipated to be longer than what is observed by a sensor, as an observing system will have difficulty distinguishing concentration enhancements below its instrument's sensitivity. For examples where the super-emitter event only contained a single detection, we assume an 8.3-min shortest duration, as that represents the minimum nonzero event duration based on observations from this survey and is within the range of durations described by a previous study¹⁸.

TROPOMI flux inversion

We use the Integrated Methane Inversion (IMI) version 2.0²² to quantify total Permian methane emissions during the study period, using TROPOMI observations from the blended TROPOMI + GOSAT retrieval product²⁹. Emissions are inferred at $0.25^\circ \times 0.25^\circ$ resolution for 200 grid elements across the basin (Fig. 2c) and at coarser resolution for 16 buffer elements outside the basin, which serve to capture external emissions and pad the rectangular inversion domain (26.5°N–37°N, 97.1875°W–108.125°W). The inversion also optimizes the boundary conditions along the four cardinal edges of the domain. We use the IMI 2.0 default prior emission estimates and assume lognormal error statistics on emissions^{22,30}. The IMI setup in this study was configured as part of a larger analysis³¹, where the inferred or satellite-derived emission estimate for one week is used to update the prior estimate for the following week's inversion. Previous study have shown that weekly emissions derived from IMI runs in this continuously updating prior mode become insensitive to the original choice of prior after 8 weeks of assimilation²¹. The IMI setup described here was initialized several years before the time period of this study³¹. We use the default IMI 2.0 values for prior errors (a uniform geometric standard deviation of 2 for all emission elements), observational errors (15 ppb), and regularization parameter ($\gamma = 1$). IMI emission estimates described in this study represent an estimated total flux – i.e., emissions from all potential sources and sectors within the regional domain described in this study, which in the Permian basin is dominated by oil and gas.

Data availability

Plume datasets are generally available via Carbon Mapper's Public Data Portal (data.carbonmapper.org). TROPOMI XCH4 data is available via the Registry of Open Data on Amazon Web Services (<https://registry.opendata.aws/sentinel5p/>). Source Data to reproduce figures are deposited in a Zenodo public repository³².

Code availability

The IMI source code is available online (<https://carboninversion.com/>). Source code to reproduce figures and analyses in this study is deposited in a Zenodo public repository³².

References

1. U.S. Environmental Protection Agency Standards of performance for new, reconstructed, and modified sources and emissions guidelines for existing sources: oil and natural gas sector climate review. *Fed. Regist.* **40**, CFR Part 60 (2024). Available at <https://www.federalregister.gov/documents/2024/03/08/2024-00366> (accessed 10 Mar 2025).
2. Sherwin, E. D. et al. US oil and gas system emissions from nearly one million aerial site measurements. *Nature* **627**, 328–334 (2024).
3. Naus, S. et al. Assessing the relative importance of satellite-detected methane superemitters in quantifying total emissions for oil and gas production areas in Algeria. *Environ. Sci. Technol.* **57**, 19545–19556 (2023).
4. Lauvaux, T. et al. Global assessment of oil and gas methane ultra-emitters. *Science* **375**, 557–561 (2022).
5. Cusworth, D. H. et al. Strong methane point sources contribute a disproportionate fraction of total emissions across multiple basins in the United States. *Proc. Natl Acad. Sci. USA* **119**, e2202338119 (2022).
6. Pandey, S. et al. Relating multi-scale plume detection and area estimates of methane emissions: a theoretical and empirical analysis. *Environ. Sci. Technol.* **59**, 7931–7947 (2025).
7. Omara, M. et al. Methane emissions from US low-production oil and natural gas well sites. *Nat. Commun.* **13**, 2085 (2022).
8. Williams, J. P. et al. Small emission sources disproportionately account for a large majority of total methane emissions from the US oil and gas sector. *EGUsphere* 2024 **1**, 31 (2024).
9. Chen, Z. et al. Comparing continuous methane monitoring technologies for high-volume emissions: a single-blind controlled release study. *ACS ES&T Air* <https://doi.org/10.1021/acsestair.4c00015> (2024).
10. Conrad, B. M., Tyner, D. R., Li, H. Z., Xie, D. & Johnson, M. R. A measurement-based upstream oil and gas methane inventory for Alberta, Canada reveals higher emissions and different sources than official estimates. *Commun. Earth Environ.* **4**, 416 (2023).
11. Johnson, M. R., Conrad, B. M. & Tyner, D. R. Creating measurement-based oil and gas sector methane inventories using source-resolved aerial surveys. *Commun. Earth Environ.* **4**, 139 (2023).
12. Kunkel, W. M. et al. Extension of methane emission rate distribution for Permian Basin oil and gas production infrastructure by aerial LiDAR. *Environ. Sci. Technol.* **57**, 12234–12241 (2023).
13. Cusworth, D. H. et al. Intermittency of large methane emitters in the Permian Basin. *Environ. Sci. Technol. Lett.* **8**, 567–573 (2021).
14. Chen, Y. et al. Quantifying regional methane emissions in the New Mexico Permian Basin with a comprehensive aerial survey. *Environ. Sci. Technol.* **56**, 4317–4323 (2022).
15. Sherwin, E. et al. Comprehensive aerial surveys find a reduction in Permian Basin methane intensity from 2020–2023. SSRN Preprint <https://doi.org/10.2139/ssrn.5087216> (2024).
16. El Abbadi, S. H. et al. Technological maturity of aircraft-based methane sensing for greenhouse gas mitigation. *Environ. Sci. Technol.* **58**, 9591–9600 (2024).

17. U.S. Environmental Protection Agency. Petroleum and natural gas systems subpart W: Greenhouse Gas Reporting Program (2024). Available at https://www.epa.gov/system/files/documents/2025-01/w_petroleumnaturalgassystems_infosheet_2024.pdf (accessed 6 Feb 2025).
18. Yang, S. L. & Ravikumar, A. P. Assessing the performance of point sensor continuous monitoring systems at midstream natural gas compressor stations. *ACS ES&T Air* **2**, 466–475 (2025).
19. Ayasse, A. K. et al. Performance and sensitivity of column-wise and pixel-wise methane retrievals for imaging spectrometers. *Atmos. Meas. Tech.* **16**, 6065–6074 (2023).
20. Veefkind, J. P. et al. TROPOMI on the ESA sentinel-5 precursor: a GMES mission for global observations of atmospheric composition. *Remote Sens. Environ.* **120**, 70–83 (2012).
21. Varon, D. J. et al. Continuous weekly monitoring of methane emissions from the Permian Basin by inversion of TROPOMI satellite observations. *Atmos. Chem. Phys. Discuss.* **2022**, 1–26 (2022).
22. Estrada, L. A. et al. Integrated Methane Inversion (IMI) 2.0: an improved research and stakeholder tool for monitoring total methane emissions worldwide. *EGUsphere* **2024** **1**, 31 (2024).
23. Barkley, Z. R., Davis, K. J., Miles, N. L. & Richardson, S. J. Examining daily temporal characteristics of oil and gas methane emissions in the Delaware Basin using continuous tower observations. *J. Geophys. Res. Atmos.* **130**, e2024JD042050 (2025).
24. Lyon, D. R. et al. Concurrent variation in oil and gas methane emissions and oil price during the COVID-19 pandemic. *Atmos. Chem. Phys.* **21**, 6605–6626 (2021).
25. Warren, J. D. et al. Sectoral contributions of high-emitting methane point sources from major US onshore oil and gas producing basins using airborne measurements from MethaneAIR. *EGUsphere* **2024**, 1–22 (2024).
26. Guanter, L. et al. Remote sensing of methane point sources with the MethaneAIR airborne spectrometer. *EGUsphere* **2025**, 1–22 (2025).
27. Zimmerle, D., Dileep, S. & Quinn, C. Unaddressed uncertainties when scaling regional aircraft emission surveys to basin emission estimates. *Environ. Sci. Technol.* **58**, 6575–6585 (2024).
28. Schubert, E., Sander, J., Ester, M., Kriegel, H. P. & Xu, X. DBSCAN revisited, revisited: why and how you should (still) use DBSCAN. *ACM Trans. Database Syst.* **42**, 1–21 (2017).
29. Balasus, N. et al. A blended TROPOMI+GOSAT satellite data product for atmospheric methane using machine learning to correct retrieval biases. *Atmos. Meas. Tech.* **16**, 3787–3807 (2023).
30. Hancock, S. E. et al. Satellite quantification of methane emissions from South American countries: a high-resolution inversion of TROPOMI and GOSAT observations. *EGUsphere* **2024**, 1–33 (2024).
31. Varon, D. J. et al. Seasonality and declining intensity of methane emissions from the Permian and nearby US oil and gas basins. *Environ. Sci. Technol.* **59**, 16021–16033 (2025).
32. Cusworth, D. Data and code to accompany “Duration of super-emitting oil and gas methane sources”. *Zenodo* <https://doi.org/10.5281/zenodo.17862303> (2024).

Acknowledgments

The Carbon Mapper team acknowledges the support of their sponsors, including the High Tide Foundation, Bloomberg Philanthropies, and other philanthropic donors. Portions of the Carbon Mapper work were funded by the NASA Carbon Monitoring System. The Global Airborne Observatory (GAO) is managed by the Center for Global Discovery and Conservation Science at Arizona State University. The GAO is made possible by support from private foundations, visionary individuals, and Arizona State University. Work by E.D.S. and S.C.B. was supported by the California Energy Commission (SUMMATION project, agreement

number PIR-17-015). It does not necessarily represent the views of the Energy Commission, its employees, or the State of California. The Energy Commission, the State of California, its employees, contractors, and subcontractors make no warranty, express or implied, and assume no legal liability for the information in this report; nor does any party represent that the use of this information will not infringe upon privately owned rights. This paper has not been approved or disapproved by the California Energy Commission, nor has the California Energy Commission passed upon the accuracy or adequacy of the information in this paper. This manuscript has been authored by authors at Lawrence Berkeley National Laboratory under Contract No. DE-AC02-05CH11231 with the U.S. Department of Energy. The U.S. Government retains, and the publisher, by accepting the article for publication, acknowledges, that the U.S. Government retains a non-exclusive, paid-up, irrevocable, world-wide license to publish or reproduce the published form of this manuscript, or allow others to do so, for U.S. Government purposes.

Author contributions

D.H.C. designed the study, performed the main analysis, and wrote the manuscript. D.B., A.A., and R.M.D. performed additional analyses of plume datasets. G.P.A. and J.H. acquired GAO data. D.J.V. performed the TROPOMI regional flux inversion. E.D.S. and S.C.B. performed additional statistical and uncertainty analyses. D.B., A.A., R.M.D., G.P.A., J.H., D.J.V., E.D.S., and S.C.B. provided feedback on the manuscript.

Competing interests

The authors declare no competing interests.

Additional information

Supplementary information The online version contains supplementary material available at <https://doi.org/10.1038/s41467-026-68804-7>.

Correspondence and requests for materials should be addressed to Daniel H. Cusworth.

Peer review information *Nature Communications* thanks the anonymous reviewers for their contribution to the peer review of this work. A peer review file is available.

Reprints and permissions information is available at <http://www.nature.com/reprints>

Publisher's note Springer Nature remains neutral with regard to jurisdictional claims in published maps and institutional affiliations.

Open Access This article is licensed under a Creative Commons Attribution-NonCommercial-NoDerivatives 4.0 International License, which permits any non-commercial use, sharing, distribution and reproduction in any medium or format, as long as you give appropriate credit to the original author(s) and the source, provide a link to the Creative Commons licence, and indicate if you modified the licensed material. You do not have permission under this licence to share adapted material derived from this article or parts of it. The images or other third party material in this article are included in the article's Creative Commons licence, unless indicated otherwise in a credit line to the material. If material is not included in the article's Creative Commons licence and your intended use is not permitted by statutory regulation or exceeds the permitted use, you will need to obtain permission directly from the copyright holder. To view a copy of this licence, visit <http://creativecommons.org/licenses/by-nc-nd/4.0/>.

© The Author(s) 2026